Journal of Biomedical Optics

BiomedicalOptics.SPIEDigitalLibrary.org

Multispectral measurement of contrast in tissue-mimicking phantoms in near-infrared spectral range of 650 to 1600 nm

Daniel Salo
Hairong Zhang
David M. Kim
Mikhail Y. Berezin

SPIE.

Journal of Biomedical Optics 19(8), 086008 (August 2014)

Multispectral measurement of contrast in tissue-mimicking phantoms in near-infrared spectral range of 650 to 1600 nm

Daniel Salo, Hairong Zhang, David M. Kim, and Mikhail Y. Berezin*
Washington University School of Medicine, Department of Radiology, 510 S. Kingshighway, St. Louis, Missouri 63130, United States

Abstract. In order to identify the optimal imaging conditions for the highest spatial contrast in biological tissue, we explored the properties of a tissue-mimicking phantom as a function of the wavelengths in a broad range of near-infrared spectra (650 to 1600 nm). Our customized multispectral hardware, which featured a scanning transmission microscope and imaging spectrographs equipped with silicon and InGaAs charge-coupled diode array detectors, allowed for direct comparison of the Michelson contrast obtained from a phantom composed of a honeycomb grid, Intralipid, and India ink. The measured contrast depended on the size of the grid, luminance, and the wavelength of measurements. We demonstrated that at low thickness of the phantom, a reasonable contrast of the objects can be achieved at any wavelength between 700 and 1400 nm and between 1500 and 1600 nm. At larger thicknesses, such contrast can be achieved mostly between 1200 and 1350 nm. These results suggest that distinguishing biological features in deep tissue and developing contrast agents for *in vivo* may benefit from imaging in this spectral range. [DOI: 10.1117/1.JBO.19.8.086008]

Keywords: multispectral; near-infrared; extended near-infrared; second optical window; Michelson contrast; phantom.

Paper 140325PR received May 21, 2014; revised manuscript received Jul. 14, 2014; accepted for publication Jul. 16, 2014; published online Aug. 7, 2014.

1 Introduction

The depth penetration of light in biological tissue is a central theme in *in vivo* optical imaging. Larger depth penetration while maintaining sufficient contrast is one of the major objectives for noninvasive diagnosis. In thin tissue slices (micrometers), where scattering is not critical, visible light is typically utilized. In thick tissue, scattering becomes the predominant problem and near-infrared (NIR) photons are utilized to alleviate the scattering effect. Within the NIR range, two optical windows are generally recognized: a traditional NIR window I (650 to 950 nm) and window II (950 to 1600 nm), also known as short-wave infrared. Since both windows are within the NIR spectral range, the second window has also been called extended NIR (exNIR)[1,2] to differentiate it from the traditional NIR wavelengths.

Optical imaging in the traditional NIR is well established and relies on a variety of contrast mechanisms, such as the scattering properties of heterogeneous tissues,[3] endogenous chromophores, such as hemoglobin[4] and melanin,[5] or exogenous contrast agents, including fluorescent NIR dyes,[6,7] nanoparticles,[8] quantum dots[9,] or far-red fluorescent proteins.[10] In the exNIR, scattering is less pronounced, and the contrast relies on a different set of endogenous chromophores, mostly water and lipids.[2] The field of exogenous fluorophores in exNIR emerged just several years ago. It is rapidly growing and currently includes single-wall carbon nanotubes,[11] quantum dots,[12–14] neodymium-doped nanoparticles,[15] and cyanine dyes.[16]

Choosing an imaging technique and developing new contrast agents demand knowledge of tissue transparency at different wavelengths. Currently, this information is well established in NIR but is vague in the exNIR range.[17,18] Two tissue parameters, scattering and absorption, govern photon transport in tissue. At longer wavelengths, scattering decreases in accordance with the Mie theory, which leads to higher photon penetration and light transmission. At the same time, the absorption is changing and exhibiting particular absorption bands and reflects tissue composition in accordance with the Beer-Lambert law. An anisotropy factor further contributes to the complexity of the optical properties. Overall, this complexity makes the prediction of the transparency at different wavelengths difficult and requires significant experimental evidence. We approached this issue through quantitative measurements of Michelson contrast as a function of wavelength. Lower contrast would suggest shallow light penetration, while higher contrast would indicate better transparency of the tissue and, therefore, would be more suitable for deep imaging.

The measurements across a broad range of 650 to 1600 nm are challenging since they require at least two types of detectors and an almost identical imaging configuration for both spectral ranges (NIR and exNIR). Such configurations are not routinely available on conventional imagers. In this work, we present a multispectral imaging system and an algorithm allowing for direct comparison of the contrast at different wavelengths from 650 to 1600 nm. With this system, we explored the transmission of tissue-mimicking phantoms and identified the spectral bands where the contrast is the highest.

*Address all correspondence to: Mikhail Y. Berezin, E-mail: berezinm@mir.wustl.edu

0091-3286/2014/$25.00 © 2014 SPIE

2 Experimental Part

2.1 *Instrument Design*

The design of the imaging instrument is shown in Fig. 1. The imager was based on an Olympus BX51 microscope equipped with a tri-axis PC-controlled stage (Märzhäuser Wetzlar GmbH & Co, Wetzlar, Germany). A 100-W halogen lamp (Olympus Corp., Tokyo, Japan) with the IR filter removed was used as a source of continuous broadband light that was passed through a condenser. Transmitted light was collected with a PlanC 4× objective (Olympus) with a relatively uniform transmission in the studied range. An Infinity3-1 color camera (Lumenera Inc., Ottawa, Canada) was used for adjusting the height of the stage so that the image is in focus with a particular objective and for setting the region of interest for map acquisition. Following the objective and beamsplitter, a pinhole (400 μm) was placed to attenuate the uncollimated light. The choice of the pinhole was based on our previous results as a balance between resolution and integration time.[1]

A liquid light guide (Newport Corp., Bozeman, Montana), with high transmission in the 420- to 2000-nm range, transmitted the photons to a fiber optic bundle with mirrors to reflect the photons to one of the two diode array, charge-coupled diode (CCD) cameras: the silicon (Si)-based Synapse detector (HORIBA Instruments Inc., Clifton Park, New York.) thermoelectrically cooled to −70°C, or the liquid nitrogen-cooled InGaAs detector Symphony II (Horiba). On the Si side, a 300 groove/mm, 500 grating within an identical spectrograph separated light for spectral analysis by the Synapse CCD, which has a sensitivity range of 400 to 1000 nm, providing a spectral resolution of 0.26 nm. On the InGaAs side, a 100 grove/mm, blaze 800 grating within an iHR 320 imaging spectrometer [focal length 320 mm, aperture f/4.1 (Horiba)] splits light for spectral analysis by Symphony II, which has a sensitivity range of 900 to 1600 nm, giving a spectral resolution of 1.54 nm. In this design, only one mechanical change—the rotation of the mirrors toward the direction of the detector—switches the acquisition from NIR to exNIR channel, rendering the results highly reproducible and comparable. Calibration of the monochromators was performed by using either the Raman spectrum of water for NIR or neodymium-doped glass (laser glass) for exNIR. Calibration of the mapping system was implemented using a standard microscope ruler slide with laser engraved lines. All components for data acquisition were integrated though FluorEssence software package (Horiba).

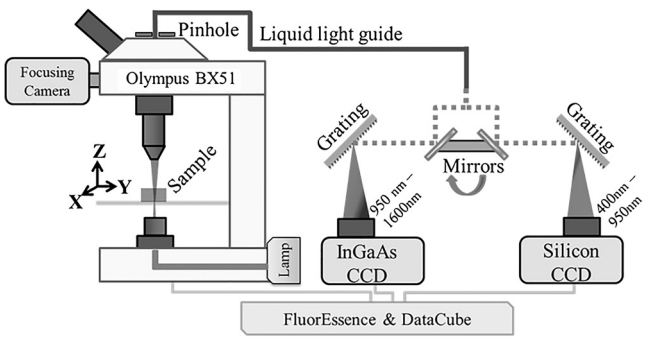

Fig. 1 Schematic of the instrument for the data acquisition and contrast measurements from 650 to 1650 nm.

2.2 *Phantom and Image Acquisition*

The tissue-mimicking phantoms used in this study were composed of Intralipid (20% fat emulsion, Fresenius Kabi AG, Bad Homburg, Germany), and India ink (2% in water, Speedball Art Products Co, Statesville, North Carolina)[19] and a honeycomb grid made from 302 stainless steel perforated with evenly spaced holes ca. 230 and 120 μm in diameter (Fotofab Inc., Chicago, Illinois). The final phantom stock solution was made from water (300 mL), Intralipid (18.75 mL), and India ink (0.615 mL) and kept at 4°C. Prior to scanning, a grid was attached beneath a plastic polystyrene Petri dish (35 mm × 10 mm). The dish was filled with different volumes of the phantom ranging from 2 to 7 mL, which corresponded to depths of ∼2.0 to ∼7.0 mm, respectively. The images were collected by focusing the objective on the grid. To minimize the edge effect, the images were recorded from the center of the Petri dish. To prevent the phantom from evaporation during the experiments, the dishes were covered with polystyrene caps. Figure 2 depicts these components and an overview of the phantom setup on the microscope.

During experimentation, the halogen lamp passed broadband light through the grid, the Petri dish, the phantom, and then into the optical instrument, where a spectrum was captured. The background spectrum was collected with no phantom. The settings, which include the step of the stage movement (10 μm), integration time (0.2 to 2 s), slit width (3 to 35 nm), and scan area (500 × 500 μm), were specified, and either the InGaAs CCD or the Si CCD was chosen to detect the light transmitted through the sample.

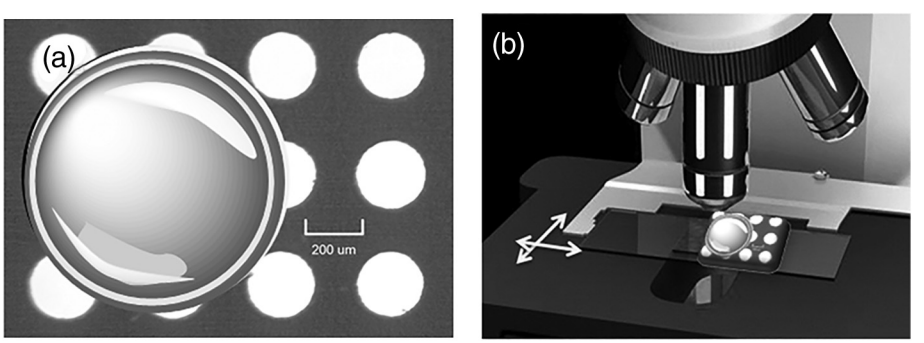

Fig. 2 (a) Phantom for the study is made from a Petri dish filled with Intralipid and India ink placed on the top of the grid holes ∼230 micron in diameter (not on the same scale) (b) Arrangement on the microscope.

2.3 *Data Processing*

The spectrum of each pixel was relayed to the custom MATLAB® program DataCube 1.0, the graphical user interface (GUI) of which is shown in Fig. 3. The Transmission Image panel on the right displays a slice of the data cube with all pixels at one wavelength, while the Spectrum of Single Pixel panel at the left shows all wavelengths for one pixel. In addition, the Wavelength Divide scroll bar at the bottom right allowed the viewer to divide out a particular wavelength from the image. The latter feature allows more advanced data analysis and is reserved for future studies.

In order to calculate contrast from the raw pixel spectra, the MATLAB® code performs several manipulations. First, all phantom spectra were divided by their respective background spectra (empty Petri dish) to normalize the data. Then, the resulting spectra were arranged into a data cube of two-dimensional images at various wavelengths. These spectra can be viewed graphically using the scroll bar titled Wavelength Control and can be multiplied by a constant using the scroll bar titled Constant Multiply to enhance the image by zooming into the scale of intensity. The Save Mask button separates the pixels into light, dark, and gray categories. The light category contains pixel intensities greater than one standard deviation from the mean pixel intensity, while the dark category contains pixel intensities less than one standard deviation from the mean pixel intensity; the gray category includes all other pixels in between. A graphical example of a mask is shown in Fig. 3. The Calculate Contrast button of the code averages the light and dark pixels and inputs them into an adapted Michelson expression [Eq. (1)] for the contrast.[17,20]

$$\text{Contrast}(\lambda) = \frac{I_{\max}(\lambda) - I_{\min}(\lambda)}{I_{\max}(\lambda) + I_{\min}(\lambda)}. \quad (1)$$

where $I_{\min}(\lambda)$ and $I_{\max}(\lambda)$ are the intensities of the light and dark areas of the two-dimensional image at each wavelength, respectively. Obtained data sets were smoothed using a Savitzky-Golay digital filter.

A contrast value of 0 signifies no contrast in the image, while a contrast value of 1 signifies the maximum contrast. Figure 3 shows a graphical example of a set of contrast values for a phantom at a depth of 5.5 mm.

3 Results and Discussion

3.1 *System Validation*

Developing the instrument in Fig. 1 involved eliminating filtering effects from all optical components that would alter the integrity of the results. We have previously described that some objectives with high transmission in the NIR showed very low to negligible transmission at wavelengths beyond 800 nm.[1] The intense search for objectives with uniform light transmission across the broad spectral range from 650 to 1600 nm led to the PlanC objectives that lack a wavelength-specific coating. Other components (fiber optics, light guides, filters, beamsplitters, and mirrors) have also been tested and selected based on their transmission in the studies' range.

3.2 *Validation of the Approach: Contrast Measurements with Blank Phantom*

Optical contrast is a direct way of measuring a combined set of biological parameters, including tissue composition (absorption, scattering). Michelson contrast is often used in optical imaging and vision science[21–23] along with other several metrics, such as a simple contrast ratio (ratio dark to light) and clinically relevant Weber contrast.[24] Michelson contrast is a method of choice for

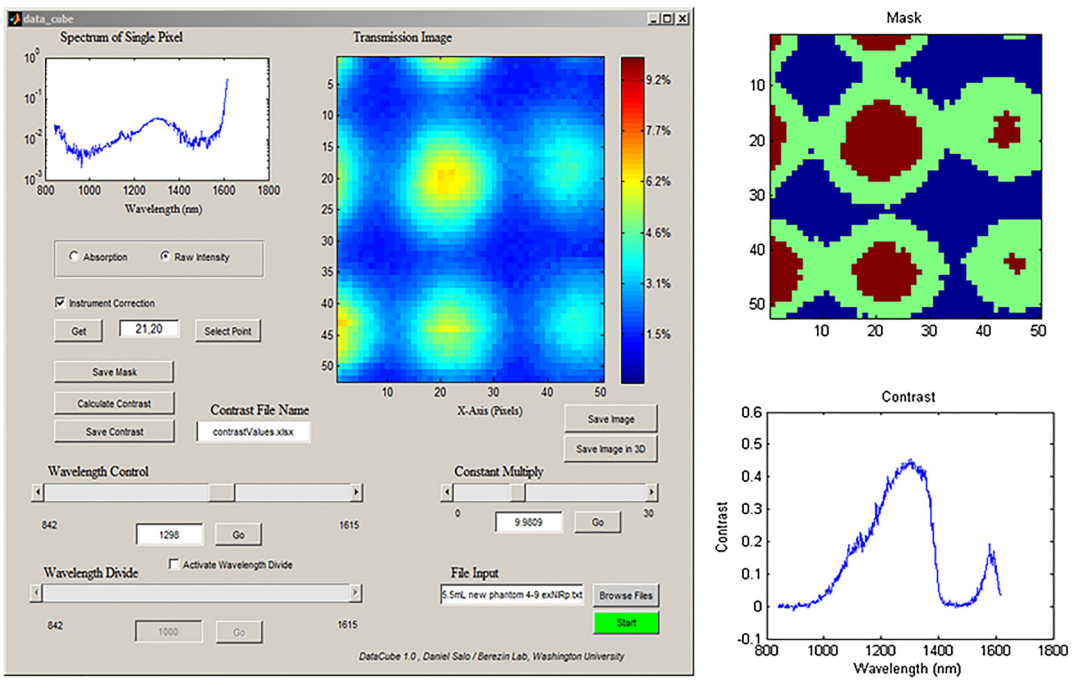

Fig. 3 The MATLAB® GUI for DataCube 1.0. The software allows slicing of the multispectral data, calculates the mask, and evaluates Michelson contrast across the image. The example is given for a phantom with grid diameter of 230 μm at depth of 5.5 mm.

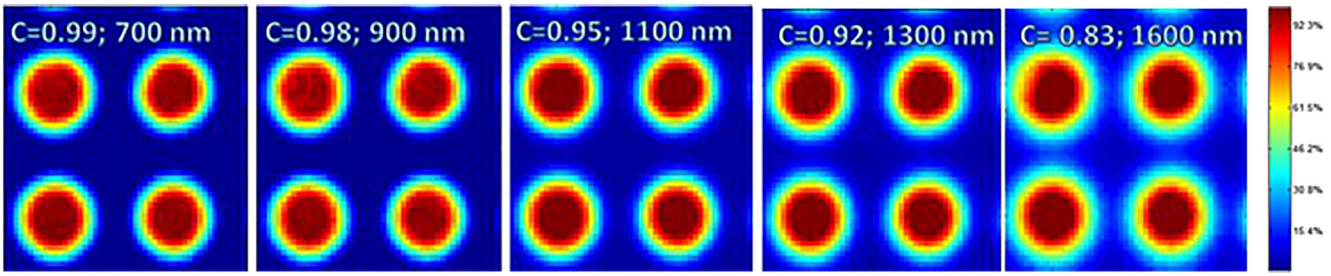

Fig. 4 Images of blank honeycomb grid phantom (230 μm diameter) at high photon count (>10,000) at different wavelengths showing dependence of the contrast from 0.99 at 650 nm to 0.83 at 1600 nm.

quantitative contrast evaluation when the contrast of grids and other patterns need to be assessed.

Measurements of the contrast of the blank phantom (grid only, no Intralipid/ink) were performed first to validate the setup and algorithm as well as to identify the effect of the wavelength and photon count on the contrast values. Under ideal conditions (no scattering and absorption, and sufficient photon count), the contrast value should be close to 1.0, the theoretical maximum at all wavelengths. Indeed, with sufficient photon collection, the contrast was close to unity for the blank phantom in the range from 650 to 1000 nm using an Si CCD. Expectedly, the contrast became somewhat lower at longer wavelengths, demonstrating a linear decrease from 0.99 at 650 nm to 0.84 at 1600 nm as illustrated in Fig. 4.

The effect of the photon count on the contrast was more significant. Similar to that of human vision, where an insufficient luminance lowers the contrast,[18] a low photon count by the detectors also resulted in a lower contrast. In these experiments, we controlled the photon count with the integration time; other parameters with the exception of the detector type were identical. With a high photon count (>10,000), the contrast values for both detectors were close to unity, as mentioned earlier. At a low photon count (<500), the contrast diminished for both detectors (Fig. 5) and was close to zero, the theoretical minimum, when no light was detected (not shown).

The contrast critically depends on the size of the object (a honeycomb grid in this study), as illustrated in Fig. 6. A finer grid (holes' diameter ~120 μm) shows significantly lower contrast values for all measured wavelengths than a coarser grid (holes at 230 μm diameter). However, the shapes of the contrast-wavelength curves for fine and coarse grids were comparable, sharing similar features and patterns and were largely independent of the grid size.

3.3 *Contrast Measurements with the Tissue-Mimicking Phantom*

The number of photons with a moderate phantom depth (2 to 4 mm) was kept within 600 to 1000 photons per measurement at the highest level of transmission (900 nm for the Si detector and 1300 nm for the InGaAs detector). For thicker samples (>4 mm), retaining this photon count was impossible without significantly increasing the scanning time or increasing the slits, which would result in the loss of spectral resolution. Consequently, the instrument was set to collect at least 100 photons at the highest channel. For each depth, identical conditions for Si and InGaAs detections (integration time, slits) were maintained. Representative images of the phantoms at 2.5 and 5 mm depths are shown in Fig. 7. At 2.5 mm, the holes in the grid are clearly seen for a wavelength as low as 800 nm. At larger depths, the holes can only be well recognized at 1200 nm with the best contrast at 1300 nm. These results illustrate the advantage of the imaging at longer wavelength: despite the increase in the absorption coefficients of water and lipids compared to 700

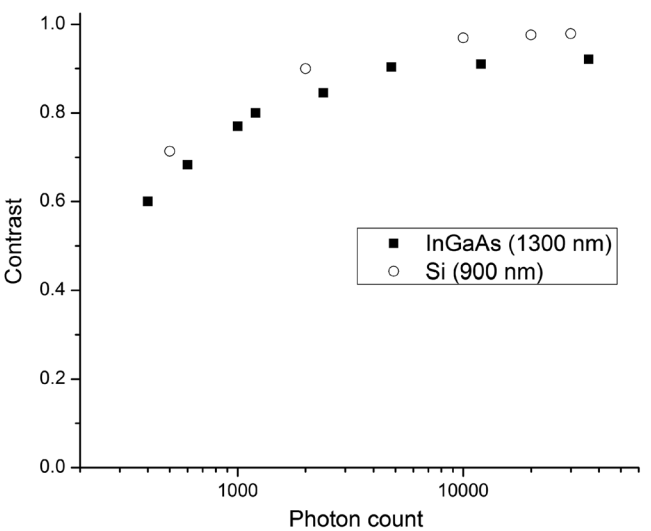

Fig. 5 Calculated contrast as a function of photon counts at two representative wavelengths. Grid 230 μm.

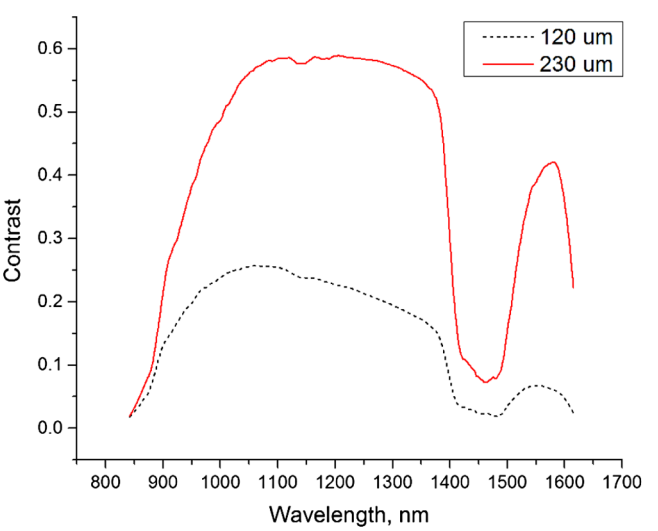

Fig. 6 Calculated contrast as a function of wavelength using grids of different size. Phantom thickness: –3 mm.

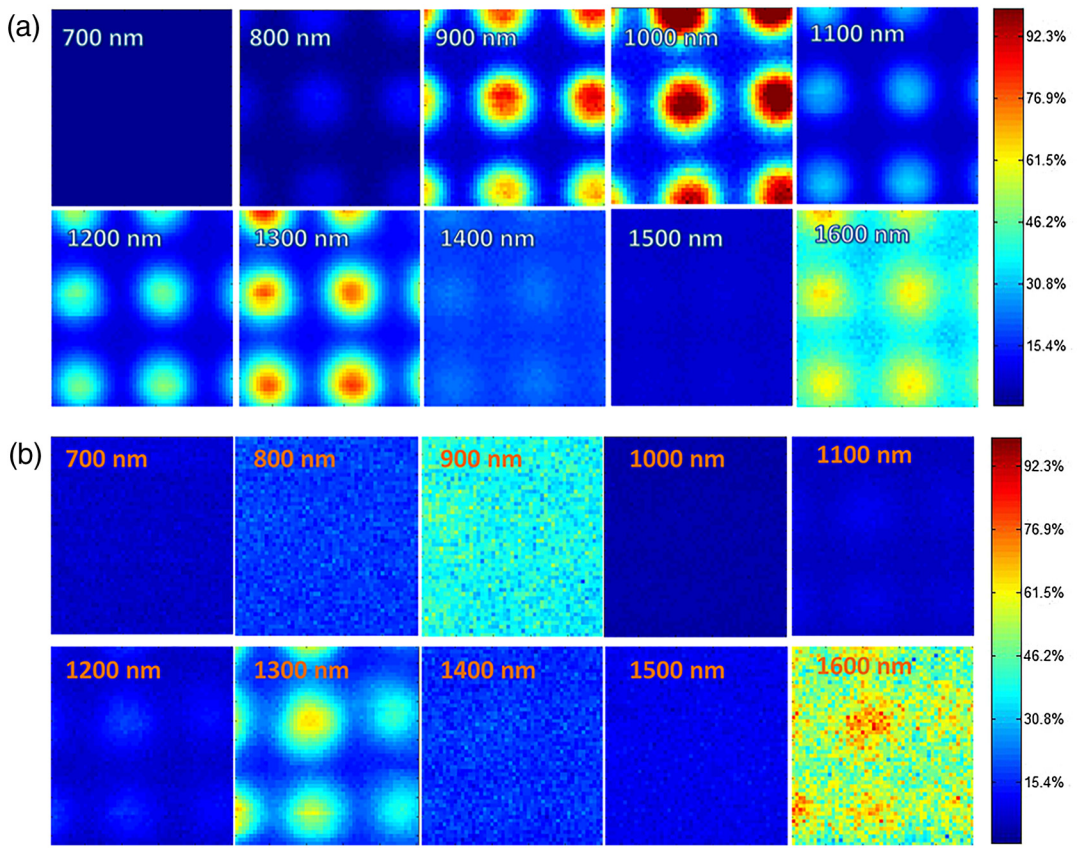

Fig. 7 Images of the honeycomb grid with Intralipid/India ink phantom (diameter 230 μm) at the depth of (a) 2.5 mm and (b) 5.0 mm (bottom) at representative wavelengths. At low depths, the holes are clearly seen with high contrast starting from 800 nm. At larger depths, the image cannot be seen below 1100 nm. The strongest contrast is seen at 1300 nm. Red color corresponds to higher light transmission.

to 900 nm, the contrast is substantially higher due to diminishing scattering.

Quantitative contrast was measured from the images, and their wavelength dependence is shown in Fig. 8. The graphs for the two different detectors are shown separately. Increased noise and lower contrast beyond 1025 nm signify lower sensitivity of the Si CCD (due to low count effect, see Sec. 3.2). Similarly, a lower sensitivity of the InGaAs CCD below 950 nm and above 1600 nm explains a lower contrast at these wavelengths.

The graph presented in Fig. 8 provides rich information regarding the transmission of the light through a tissue-mimicking phantom. At low depths, reasonable contrast (contrast > 0.1) can be achieved at any wavelength within 750 and 1400 nm, and 1550 and 1600 nm. Relatively good contrast at ~1550 nm explains the recent usage of this wavelength in deep tissue imaging using ytterbium and erbium codoped nanoparticles[25] and in two-photon imaging with NIR fluorescent dyes.[26,27] At greater depths (>6 mm), this level of contrast can be achieved only within a narrow spectral band of 1200 to 1350 nm. The shape of this band correlates with the absorption spectra of water and lipids (Fig. 9). The maximum contrast at ca. 1300 nm matches the minima in their corresponding absorption spectra. At wavelengths <1200 nm, absorption is higher and scattering apparently dominates. At wavelengths >1350 nm, a large absorbance from water, and, to a lesser degree, lipids, becomes dominant. Overall, these absorption and scattering factors lead to an insufficient amount of light reaching the detector, thus effectively blocking the light transmission and decreasing the contrast.

The presented study utilized a standard Intralipid/India ink solution as a phantom. Such a solution has been mostly used as a tissue-simulating phantom in the NIR window I (600 to 1000 nm), since it has optical properties similar to tissue when diluted to 0.5 to 2% by volume.[28] Troy and Thennadil found that this phantom can also be used in the exNIR range, for mimicking the optical properties of skin.[17] Our phantom also includes India ink—a black pigment made from carbon particles to mimic blood. This pigment has some scattering components due to a small fraction of micron-sized particles[29] and absorbs light in a broad spectral range. India ink apparently has no distinctively known absorption bands in the NIR and exNIR[30,31] and, therefore, does not contribute to the shape of the contrast. Our data demonstrate that the highest contrast with an Intralipid/India ink phantom at large depths can be achieved at 1300 nm. However, we expect that contrast as a function of wavelength will be different for real biological tissue and will depend on the type of the tissue. Moreover, due to tissue heterogeneity and the variety of contributing chromophores, the tissue could be differentiated based on its composition, thus opening up important applications in clinical settings. Recently, a relevant article on this exact topic using exNIR for differentiating nerve tissue from adipose has been published.[32] Identification of the optical window through contrast measurements in a variety of biologic tissues using the described approach is the current focus of our research and will provide

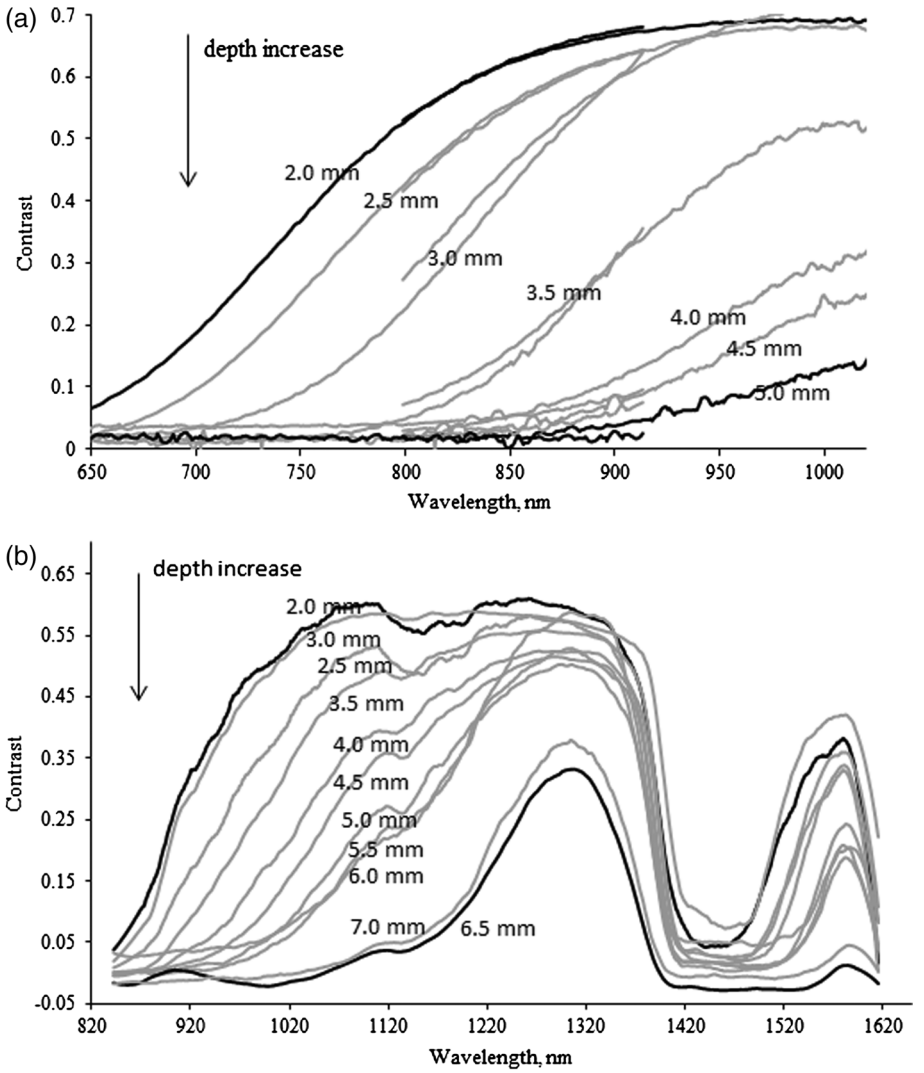

Fig. 8 Contrast data across wavelengths from 650 to 1600 nm and thicknesses from 2 to 7 mm for phantoms with grid diameter of 230 μm. (a) Si detector, two ranges (650 to 910 nm and 800 to 1100 nm) were overlapped. (b) InGaAs detector 850 to 1620 nm. Numbers are showing the depth of the phantom.

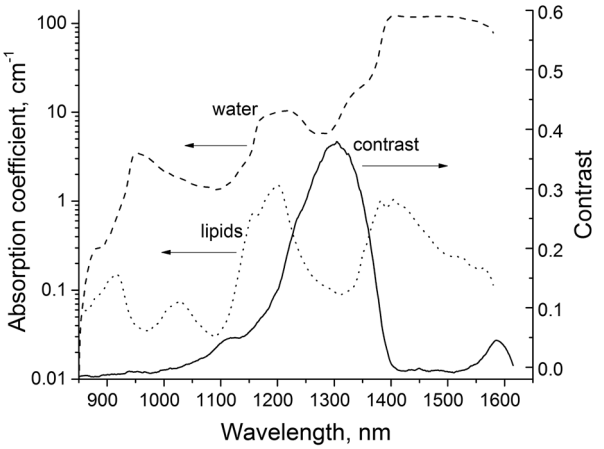

Fig. 9 Contrast correlates with the absorption spectra of water and lipids. Contrast at 7 mm phantom depth using phantoms with 230 μm grid. The data for absorption are taken from Ref. 2.

critical information regarding tissue transparency for imaging and contrast development.

4 Summary

Using a scanning microscope connected to imaging spectrograph equipped with Si and InGaAs CCD diode array detectors, we, for the first time, evaluated contrast in the broad range of NIR spectral range (650 to 1600 nm). Using our tissue-mimicking phantom, we demonstrated that at low depths, a reasonably good contrast can be achieved at any wavelength between 650 and 1400 nm and between 1500 and 1625 nm. At larger depths, such a contrast can be reached only between 1200 and 1350 nm. These results suggest that features in deep tissue may benefit from the development of imaging techniques and *in vivo* contrast agents in this spectral range. Further work will explore the effect of wavelength on contrast of different biological tissues.

Acknowledgments

We thank the Washington University Optical Spectroscopy Core (NIH 1S10RR031621-01) for spectroscopy measurements and Horiba Jobin Yvon Inc. for great help with the instrumentation. We also thank the National Heart, Lung and Blood Institute as a Program of Excellence in Nanotechnology (HHSN268201000046C), Amgen foundation (D. S.), and SURF program (H. Z.) for funding.

References

1. D. Salo et al., "Wavelength-dependent measurement of contrast in NIR and extended NIR spectral range (650–1600 nm) in phantoms," *Proc. SPIE* **8940**, 89400O (2014).
2. Q. Cao et al., "Multispectral imaging in the extended near-infrared window based on endogenous chromophores," *J. Biomed. Opt.* **18**(10), 101318 (2013).
3. V. Turzhitsky et al., "Spectroscopy of scattered light for the characterization of micro and nanoscale objects in biology and medicine," *Appl. Spectrosc.* **68**(2), 133–154 (2014).
4. A. Devor et al., "Frontiers in optical imaging of cerebral blood flow and metabolism," *J. Cereb. Blood Flow Metab.* **32**(7), 1259–1276 (2012).
5. Y. Dancik et al., "Use of multiphoton tomography and fluorescence lifetime imaging to investigate skin pigmentation *in vivo*," *J. Biomed. Opt.* **18**(2), 026022 (2013).
6. T. P. Gustafson et al., "Defining a polymethine dye for fluorescence anisotropy applications in the near-infrared spectral range," *Chemphyschem* **13**(3), 716–723 (2012).
7. S. Achilefu et al., "Novel receptor-targeted fluorescent contrast agents for *in vivo* tumor imaging," *Invest. Radiol.* **35**(8), 479–485 (2000).
8. T. P. Gustafson et al., "Blood triggered rapid release porous nanocapsules," *RSC Adv.* **3**(16), 5547–5555 (2013).
9. S. Kim et al., "Near-infrared fluorescent type II quantum dots for sentinel lymph node mapping," *Nat. Biotechnol.* **22**(1), 93–97 (2003).
10. D. M. Shcherbakova and V. V. Verkhusha, "Near-infrared fluorescent proteins for multicolor *in vivo* imaging," *Nat. Methods* **10**(8), 751–754 (2013).
11. G. Hong et al., "Multifunctional *in vivo* vascular imaging using near-infrared II fluorescence," *Nat. Med.* **18**(12), 1841–1846 (2012).
12. N. Won et al., "Imaging depths of near-infrared quantum dots in first and second optical windows," *Mol. Imaging* **11**(4), 338–352 (2012).
13. C. Li et al., "*In vivo* real-time visualization of tissue blood flow and angiogenesis using Ag_2S quantum dots in the NIR-II window," *Biomaterials* **35**(1), 393–400 (2014).
14. C. Chen et al., "Cation exchange-based facile aqueous synthesis of small, stable, and nontoxic near-infrared Ag_2Te/ZnS core/shell quantum dots emitting in the second biological window," *ACS Appl. Mater. Interfaces* **5**(3), 1149–1155 (2013).
15. U. Rocha et al., "Neodymium-doped LaF(3) nanoparticles for fluorescence bioimaging in the second biological window," *Small* **10**(6), 1141–1154 (2014).
16. Z. Tao et al., "Biological imaging using nanoparticles of small organic molecules with fluorescence emission at wavelengths longer than 1000 nm," *Angewandte Chemie* **125**(49), 13240–13244 (2013).
17. T. L. Troy and S. N. Thennadil, "Optical properties of human skin in the near infrared wavelength range of 1000 to 2200 nm," *J. Biomed. Opt.* **6**(2), 167–176 (2001).
18. A. N. Bashkatov et al., "Optical properties of human skin, subcutaneous and mucous tissues in the wavelength range from 400 to 2000 nm," *J. Phys. D: Appl. Phys.* **38**(15), 2543–2555 (2005).
19. A. Q. Bauer et al., "Quantitative photoacoustic imaging: correcting for heterogeneous light fluence distributions using diffuse optical tomography," *J. Biomed. Opt.* **16**(9), 096016 (2011).
20. A. A. Michelson, *Studies in Optics*, Dover Publications, New York (1995).
21. T. Gollisch and M. Meister, "Rapid neural coding in the retina with relative spike latencies," *Science* **319**(5866), 1108–1111 (2008).
22. J.-L. Xiao, H.-J. Pan, and C.-H. Lee, "Optically micropatterned culture of adherent cells," *J. Biomed. Opt.* **17**(7), 075004 (2012).
23. E. Peli et al., "Effect of luminance on suprathreshold contrast perception," *J. Opt. Soc. Am. A* **8**(8), 1352–1359 (1991).
24. S. A. Haymes et al., "The letter contrast sensitivity test: clinical evaluation of a new design," *Invest. Ophthalmol. Vis. Sci.* **47**(6), 2739–2745 (2006).
25. M. Kamimura et al., "Near-infrared (1550 nm) *in vivo* bioimaging based on rare-earth doped ceramic nanophosphors modified with PEG-b-poly (4-vinylbenzylphosphonate)," *Nanoscale* **3**(9), 3705–3713 (2011).
26. M. Y. Berezin et al., "Two-photon optical properties of near-infrared dyes at 1.55 mum excitation," *J. Phys. Chem. B* **115**(39), 11530–11535 (2011).
27. S. Yazdanfar et al., "Multiphoton microscopy with near infrared contrast agents," *J. Biomed. Opt.* **15**(3), 030505 (2010).
28. S. T. Flock et al., "Optical-properties of Intralipid—a phantom medium for light-propagation studies," *Lasers Surg. Med.* **12**(5), 510–519 (1992).
29. S. J. Madsen, M. S. Patterson, and B. C. Wilson, "The use of India ink as an optical absorber in tissue-simulating phantoms," *Phys. Med. Biol.* **37**(4), 985–993 (1992).
30. J. R. Cook, R. R. Bouchard, and S. Y. Emelianov, "Tissue-mimicking phantoms for photoacoustic and ultrasonic imaging," *Biomed. Opt. Express* **2**(11), 3193–3206 (2011).
31. P. Di Ninni, F. Martelli, and G. Zaccanti, "The use of India ink in tissue-simulating phantoms," *Opt. Express* **18**(26), 26854–26865 (2010).
32. R. M. Schols et al., "Differentiation between nerve and adipose tissue using wide-band (350–1,830 nm) *in vivo* diffuse reflectance spectroscopy," *Lasers Surg. Med.* (2014).

Mikhail Y. Berezin is an assistant professor at the Washington University School of Medicine in St. Louis, Missouri. He is the author of more than 50 peer-reviewed papers. His current research interests include optical spectroscopy, optical imaging, and design of near-infrared contrast agents for tissue imaging and diagnostics. He is a member of SPIE and OSA.

Biographies of the other authors are not available.